Eulerian and Lagrangian coherent structures in a positive surge

L. Thomas, L. David

L. Thomas, L. David. Eulerian and Lagrangian coherent structures in a positive surge. Experiments in Fluids, 2022, 63 (2), pp.43. ⟨10.1007/s00348-022-03383-z⟩. ⟨hal-03840066⟩

Noname manuscript No.
(will be inserted by the editor)

Eulerian and Lagrangian coherent structures in a positive surge.

L. Thomas · L. David

Received: date / Accepted: date

Abstract In this paper, a positive surge is studied in the laboratory at Froude 1.5, using stereo time-resolved particle image velocimetry (stereo-PIV). To understand the flow dynamics, the coherence of the flow is studied using Lagrangian and Eulerian tools. It is analyzed using flow statistics calculated in a frame of reference moving with the surge front. Just after the breaker, the boundary layer thickens, and strong 3D perturbations appear just behind The shear layer under the free surface cannot follow the breaking front, giving rise to a flow instability that develops rapidly and invades the whole flow, interacting with the boundary layer. The analysis of the coherent structures sheds new light on the flow organisation. New quantities can be measured, such as coherent structures maximal penetration or velocity.

Keywords positive surge · coherence · Lagrangian Coherent Structures · Eulerian Coherent Structures · FTLE

1 Introduction

Positive surges are very common flows in the environment and many papers can be found in the literature about them. One interest in studying such flows is the impact that they can have on the sediment transport, modifying considerably the biological environment of the rivers. They have been reproduced in laboratories, but also in the field (see Furgerot *et al.* (2016)). For a general review on experimental results obtained in surges, it is possible to consult Chanson (2009). To complete this, a few numerical studies have been performed, such as Lubin *et al.* (2010). Positive surges are different from tidal bores, because they are not generated the same way: to generate bores, the river flow slows down progressively when the tide is rising, while surges are generated more brutally. The hydraulic jumps are usually stationnary, while surges and bores are translating, giving rise to different observation conditions, and also different boundary conditions compared to the jump velocity for a given Froude number (see for example (Yeh & Mok (1990) for visualizations with Planar Laser Induced Fluorescence (PLIF) or Lubin & Chanson (2017)).

Many studies concentrated on the free surface evolution. For example, Zheng *et al.* (2018) are studying the free surface shape as a function of the Froude number). Chanson (2009) have also shown that the wave characteristics depends on the Froude number, the width of the channel and the flow rate. A few authors have investigated turbulent properties of the flow, like Koch & Chanson (2008) (Reynolds stresses), Leng & Chanson (2016) (time lag between front arrival and maximum stress, probability distribution functions), Leng & Chanson (2017b) (scaling of free-surface and turbulent properties) and Leng & Chanson (2017a) (integral scales). The studies in Leng & Chanson (2017b) and Leng & Chanson (2017a) used 25 runs to perform ensemble statistics. They have shown that the flow is an-isotropic and unsteady. Already, Yeh & Mok (1990) have observed turbulent patches appearing behind surge fronts. Chanson (2009) have observed large

L. Thomas
Institut P'
CNRS · Université de Poitiers · ISAE-ENSMA – UPR 3346
SP2MI - Téléport 2, 11 Boulevard Marie et Pierre Curie
BP 30179
F86962 FUTUROSCOPE CHASSENEUIL Cedex
Tel.: +33-5.49.49.69.43
Fax: +33-5.49.49.74.15
E-mail: lionel.thomas@univ-poitiers.fr

Reynolds stresses near the developping shear layer. Lately, experimental studies are more focused on breaking surges, like in Wüthrich *et al.* (2020), and the bubbles formation. In Martin *et al.* (1993), Martin *et al* were also interested by surges evolving on a slope. A new complexity is emerging with the deceleration of the surge until its disappearing.

Anyway, in most experimental studies, the flow is investigated using one-point measurements, in particular Acoustic Doppler Velocimetry. Some studies were conducted with visualizations, like in Yeh & Mok (1990) or Martin *et al.* (1993)). The use of optical method to study this kind of flow is rather new. Lennon & Hill (2006) have used traditional 2D Particle Image Velocimetry (PIV), but only statistics and shear stresses have been considered, in a stationnary hydraulic jump, which is an easier case. Hornung *et al.* (1995) have used PIV to study a dam break. They have shown the presence of a shear layer at the toe, and presented a scenario of vorticity generation mechanism by surface reconnection. More recently, David *et al.* (2014) have investigated the influence of the initial conditions (turbulence intensity, boundary layer thickness) on the free-surface evolution of the surge and the turbulence in the flow.

In this paper, a new point of view on the flow is presented, using time-resolved 2D3C measurements, giving access to the spatial and temporal dynamics of the flow. In particular, the coherence of the flow is studied using Eulerian or Lagrangian representations.
In section 2, the measurement techniques are presented, and also the studied flow. In section 3, the idea of coherence is explained and several criteria are detailed such as correlations, Eulerian Coherent Structures identification (rortex) and Lagrangian Coherent Structures analysis tool (Finite Time Lyapunov Exponents (FTLE), Lagrangian descriptor). Results are presented in section 4 and finally, a conclusion is made.

2 Experimental setup

2.1 Measurement techniques

The measurement technique used in this article is presented below. A comparison is made between ground and laboratory experiments to justify the choice of the technique.

2.1.1 One-point measurements

Several techniques can be used to perform 1D temporal measurements. In the lab, Laser Doppler Velocimetry (LDV) is often used because it is non intrusive (optical method). It is based on the measurement of the Doppler frequency for a particle crossing a interference fringes inside the intersection volume of two out of phase laser beams. Among the other techniques, hot wire velocimetry performs well to get high frequency measurements. It is slightly intrusive but can be fragile. In the field, especially in the presence of sediment, Acoustic Doppler Velocimetry (ADV) is the preferred method as it is robust. The raw signal may be noisy, but it is possible to filter the data (see Chanson (2008)). An extension can be made to perform profile measurements using Acoustic Doppler Current Profiler (ADCP), with the same drawback as for ADV. In this paper, the 1D measurements are extracted directly from 2D measurements, that are presented next.

2.1.2 Planar measurements

The most commonly used measurement technique in laboratory studies is particle image velocimetry (PIV) (see Raffel *et al.* (2018)). The principle is to seed the flow with tracers that follow the flow, illuminated by a laser sheet, and make a pair of images. A mathematical treatment, mostly based on image inter-correlations, leads to the most likely displacement of small groups of particles. This method is not used for field measurements because it would require underwater cameras to be placed in the river and a laser to be used outside, which could cause safety and power supply problems. In addition, the actual flows are on a very large scale and the issue of seeding could be problematic.

In our case, the stereo particle image velocimetry (stereoPIV) measurement technique (requiring two cameras) was used. The advantage of this technique over PIV, is that all three velocity components are obtained in the measurement plane. Therefore, it gives the possibility to verify the three-dimensionality of the flow and reduces the bias on the 2D velocity components that is due to perspective. The images were recorded by two 10 bit Photron SA1 cameras, located on either side of the water channel, at an angle of about 20°. A Scheimpflug adapter was mounted on the cameras to reduce focusing problems. The laser sheet was generated using a Darwin Duo laser (30 mJ energy per double pulse). The recording was performed at a frequency of 500 Hz, leading to time-resolved measurements.

2.1.3 Time resolved measurements

When the time between two pairs of consecutive images is the same as between the two images in the pair, there is no longer a need to make pairs. The time series can then benefit from a specific processing, using the Fluid Trajectory Evaluation algorithm based on ensemble mean cross-correlation (FTEE) (see Jeon *et al.* (2014)) which also exploit the temporal continuity of the data. This algorithm was used in this study.

2.2 Experimental set-up

The measurement techniques, presented before, are applied to an experimental flow generated in a laboratory. It concerns a positive surge, also called translating hydraulic jump. It is somehow similar to a tidal bore, except that the generation is different.

The experimental setup is presented in figure 1. The channel is 8 m long and 40 cm wide. The water level is controlled with a weir at the channel end. The jump is generated using a gate, falling with a controlled velocity. At the channel entrance, on the left of the figure, a 3D convergent and several grids ensures a clean flow. The free surface level is measured with four acoustic sensors. It is used to provide a mask to PIV processing, using an average of the two central sensors, weighted by the distance from the sensors. Outside the valid measurement region, the velocity is fixed to zero. In this case, not so many bubbles are present as the front roll is of weak intensity. Also, fluorescent particles have be used as PIV tracers. These 20 μm diameter particles are made with polyamid (density 1.04) doped with rhodamine 6G. Only the fluorescent pink signal is measured by the cameras equipped with a high pass filter), avoiding the green light reflections on the free surface. Nevertheless, it is difficult to seed the flow just below the free surface. An example of image is given in figure 2. The stereoPIV spatial resolution is 2,3 mm in X and 2,0 mm in Y, leading to a 123×123 data grid. The chosen configuration corresponds to a 16,66 L/s flow rate, assured by a worm pump. The initial water height (direction y) was d_1=7,0 cm, for a mean longitudinal (direction x) velocity U_1=0,609 m/s. The jump, generated by a shutter gate, visible on the right part of the figure, was moving upstream with a velocity U_b=-0,644 m/s. The Froude number Fr_1 in the jump frame is defined classically in equation 1.

$$Fr_1 = \frac{U_1 - U_b}{\sqrt{gd_1}} \tag{1}$$

This definition doesn't take into account the presence of the boundary layer or the shear layer. It should include the β momentum coefficient defined in equation 2. The modified Froude definition would be given in equation 3.

$$\beta = \frac{\overline{(U - U_b)^2}}{(U_1 - U_b)^2} \tag{2}$$

where $\overline{(.)}$ is an averaging operator along a vertical line going from the wall to the free surface.

$$Fr_1 = \sqrt{\beta}\frac{U_1 - U_b}{\sqrt{gd_1}} \tag{3}$$

For a turbulent flow, $\beta \simeq 1$ so both definitions coincide.

In the present case, the value is $Fr_1 \simeq$ 1,5. This would correspond to an undulating tidal bore. The thickness of the upstream boundary layer is about 1.5 cm. A shear layer is also present below the free surface. Its thickness is about 2.5 cm. The mean stream-wise velocity profile is given in figure 3. In what follows, the reference length is d_1, the reference velocity is U_1 and the reference time is $\sqrt{d_1/g}$. All variables are scaled.

3 Eulerian and Lagrangian analysis tools

Coherence plays an important role in fluid mechanics, as it drives large-scale events and contains a lot of energy. Fluid particles can be considered as coherent when their dynamics are similar. In terms of dynamical systems theory, they are coherent when they evolve in the same regular orbit. In turbulent flows, the trajectory can evolve on regular orbits or on chaotic attractors, the complexity of the trajectory being proportional to the number of degrees of freedom. Even during their lifetime, particles can follow different types of trajectories: they can spend a long time on regular orbits and then be ejected on chaotic attractors. The identification of regular orbits is not an easy task because they can be complex and, in experiments, the observation is only partial. The identification of regular motions depends on the type of observation. When point measurements are made, only the temporal behavior can be studied. When the observation is spatial but sparse in time, the spatial behavior can be observed. And finally, when the observation is dense in space and time, the spatio-temporal behavior can be analyzed.

3.1 Correlations: temporal coherence

Historically, because of the limitations of measurement techniques, the first way to observe coherence was to to observe coherence was to use correlations on one or two points. The correlation is a measure of the similarity of

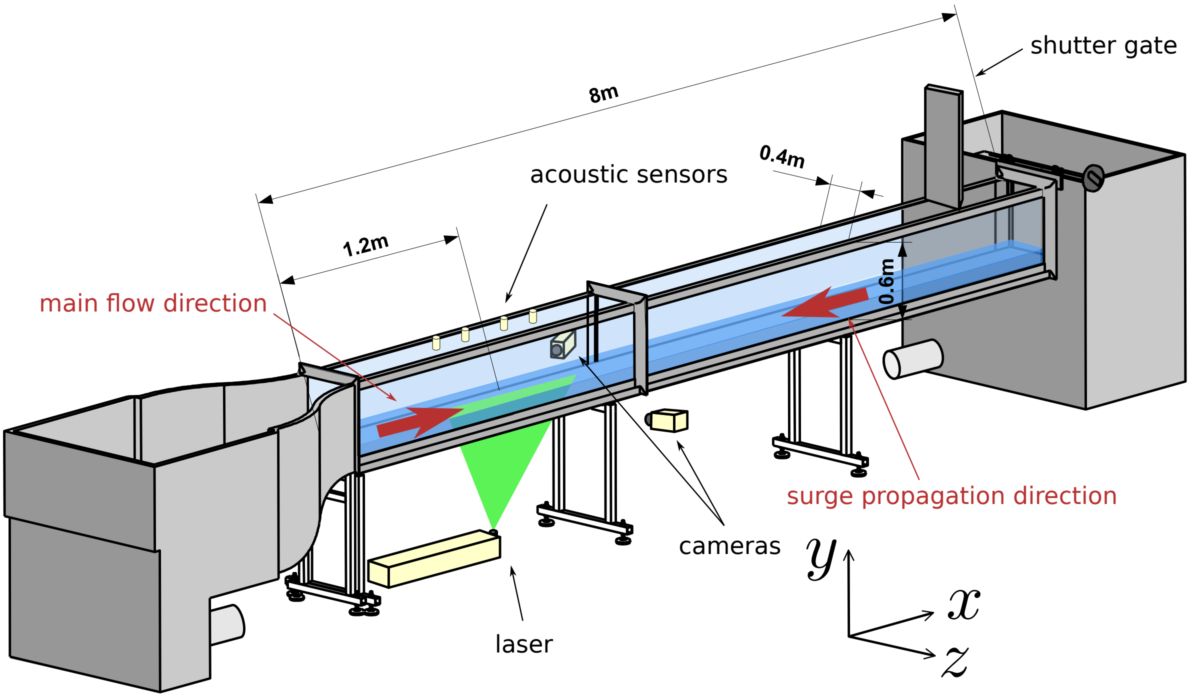

Fig. 1: Open channel flow used to generate hydraulic jumps in translation, and associated measurement devices. The main flow entrance is on the left, the shutter door to generate the surge is on the right. The surge is going from right to left. The four acoustics sensors used to measure the free-surface level (small cylinders), the laser and both cameras, represented in yellow, are fixed.

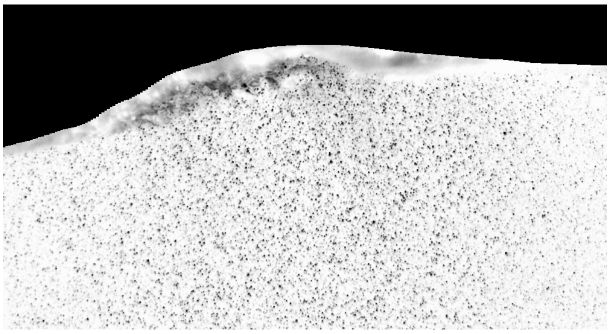

Fig. 2: Example of particle image, dewarped and masked using the acoustic sensors.

two signals. It is an Eulerian approach. The temporal evolution is observed at two points separated in space or in time. The correlation of two signals $A_1(\mathbf{x_1},\, t)$ and $A_2(\mathbf{x_2},\, t)$ is given by the equation 4.

$$A_1{*}A_2(t_1, t_2, \mathbf{x_1}, \mathbf{x_2}) = < A_1(\mathbf{x_1},\, t{-}t_1) A_2(\mathbf{x_2},\, t{-}t_2) >_T \tag{4}$$

where $< \cdot >_T$ is a temporal average on the variable t in the interval $[0;T]$. T is the observation time, that

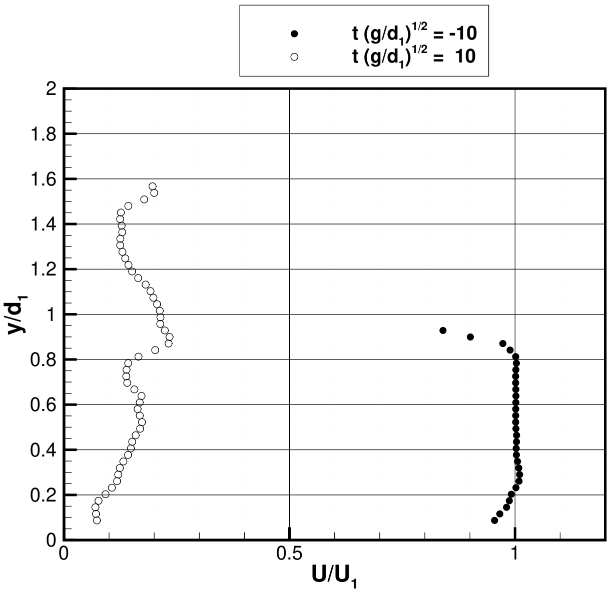

Fig. 3: Two mean velocity profiles, one taken upstream the jump, the other downstream.

should be long enough to get statistical convergence. The normalized correlation is given in equation 5.

$$C_{A_1,A_2}(t_1,t_2,\mathbf{x_1},\mathbf{x_2}) = \frac{A_1 * A_2(t_1,t_2,\mathbf{x_1},\mathbf{x_2})}{\sqrt{A_1 * A_1(t_1,t_1,\mathbf{x_1},\mathbf{x_1})}\sqrt{A_2 * A_2(t_1,t_1,\mathbf{x_1},\mathbf{x_1})}} \quad (5)$$

When $\mathbf{x_1} = \mathbf{x_2}$, the correlation is a (two times) one-point correlation. When $t_1 = t_2$, the correlation is a (one time) two-point correlation.

These correlations are usually used to study turbulent signals, with a rich dynamical content, and are calculated on the fluctuations of the signals. The fluctuations are computed as $A' = A - < A >_T$. Correlations can be also used to test the homogeneity of the flow (the correlation should depend only on $\mathbf{x_2} - \mathbf{x_1}$) and its stationnarity (the correlation should depend only on $t_2 - t_1$). Integral length scales can be defined by integrating the correlations such as in equations 6 and 7.

$$T_i(\mathbf{x_1}, t_1) = \int_0^T C_{A_1,A_2}(t_1, t_1+\lambda, \mathbf{x_1}, \mathbf{x_1})\, d\lambda \quad (6)$$

$$L_i(\mathbf{x_1}, \mathbf{e_1}, t_1) = \int_0^L C_{A_1,A_2}(t_1, t_1, \mathbf{x_1}, \mathbf{x_1} + \lambda\mathbf{e_1})\, d\lambda \quad (7)$$

where L is the observation distance and $\mathbf{e_1}$ is the observation direction (with a unit norm).

3.2 Eulerian Coherent Structures: spatial coherence

There is no universal definition of an Eulerian coherent structure (ECS) but many criteria that an ECS should respect have been defined. Some insights on the subject can be found in Günther & Theisel (2018) or Epps (2017). Originally, they should represent vortices (see the first works in Hussain (1983), Grant (1958), Jeong & Hussain (1995) or Liu (1989)). Vorticity was the first criterion that represented the instantaneous local rotation of fluid particles. There are three main drawbacks to this view: first, Eulerian criteria are based on an instantaneous view of the flow field and may not be representative of behavior that will persist over time. Second, even in a shear layer, fluid particles undergo instantaneous rotation, but they are also stretched and sheared. It can be difficult to separate these different motions. Third, a criterion for identifying a vortex must be objective (see Haller (2005)). To illustrate some concepts, a local analysis of the 2D velocity field can be performed. Consider the velocity field at a point $\mathbf{x}_c$ (see equation 8).

$$\mathbf{u}(\mathbf{x}) = \mathbf{u}(\mathbf{x_c}) + \mathbf{L_1}(\mathbf{x_c})(\mathbf{x} - \mathbf{x_c}) \quad (8)$$

Most of the criteria are based on the velocity gradient tensor $\mathbf{L_1}$ analysis. Now let's consider a short filament $\mathbf{l}$ of length l and of direction $\mathbf{e}$ ($l\mathbf{e} = \mathbf{x} - \mathbf{x_c}$). If it is passive, it is advected by the flow.The stretching $\dot{\eta}$ of the filament is given in equation 9.

$$\dot{\eta} = \frac{\dot{l}}{l} = \mathbf{e} \cdot \mathbf{L_1}\mathbf{e} \quad (9)$$

The rotation $\dot{\Gamma}\mathbf{e_z}$ of the filament is defined in equation 10.

$$\dot{\Gamma}\mathbf{e_z} = \mathbf{e} \wedge \dot{\mathbf{e}} = \mathbf{e} \wedge \mathbf{L_1}\mathbf{e} \quad (10)$$

In 2D, it is possible to calculate the vector $\dot{K}$, in complex form, $K = \dot{\eta} + i\dot{\Gamma}$ where i is the unit imaginary complex number, and $\mathbf{e} = e^{i\theta}$. The Eulerian velocity gradient tensor is written such as in equation 11.

$$\mathbf{L_1} = \begin{pmatrix} \frac{\sigma}{2} + \gamma_1 & \gamma_2 - \frac{\omega}{2} \\ \gamma_2 + \frac{\omega}{2} & \frac{\sigma}{2} - \gamma_1 \end{pmatrix} \quad (11)$$

$\sigma = \mathrm{tr}(\mathbf{L_1}) = \mathrm{div}\mathbf{u}$ represents the compression/dilatation of the fluid due to the compressibility of the flow. In hydraulics, the flow are incompressible and σ=0. ω is the vorticity. $\gamma = \sqrt{\gamma_1^2 + \gamma_2^2}$ is the shear.
A simple calculus leads to equation 12.

$$\dot{K} = \frac{\sigma + i\omega}{2} + (\gamma_1 + i\gamma_2)e^{-2i\theta} \quad (12)$$

This is a circle equation, with radius γ and center $\frac{\sigma+i\omega}{2}$ (see figure 4).

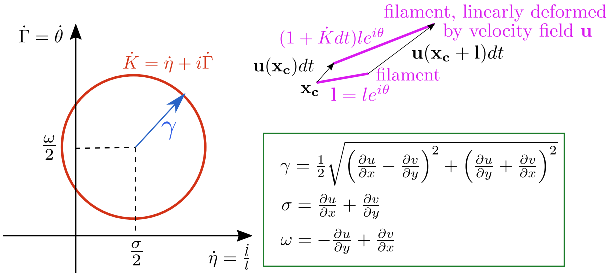

Fig. 4: Variations of $\dot{K}$ when the initial orientation of the filament θ is varying.

A necessary condition for the existence of a vortex is that, whatever the initial orientation of the filament, the rotation never disappears, so that the rotation is always in the same direction. This gives the necessary condition of the equation 13.

$$\frac{|\omega|}{2} > \gamma \quad (13)$$

One difficulty is the divergence of the velocity, which can exist even in an incompressible flow, due to the presence of noise. To cope with this, it is possible to subtract $\frac{\sigma}{2}$ from the velocity gradient tensor $\mathbf{L_1}$, where $\mathbf{I}$ is the identity tensor. In this case, all classical vortex detection criteria are identical to the 13 condition. The rotational velocity of the filament can be given by the criterion $Q^{\frac{1}{2}}$, as given in equation 14. It corresponds to a geometric mean of the minimum and maximum rotations, while the vorticity corresponds to an arithmetic mean.

$$\dot{\Gamma} = \sqrt{\left(\frac{\omega}{2}\right)^2 - \gamma^2} \tag{14}$$

Another possibility is given by the triple decomposition defined in Kolář (2007). It consists in taking only the minimum rotation of the filament, like in equation 15.

$$\dot{\Gamma} = \mathrm{sgn}(\omega)\left(\frac{|\omega|}{2} - \gamma\right) \tag{15}$$

In 3D, the rotation of a filament of direction $\mathbf{e}$ is given by the equation 16.

$$\dot{\Gamma}\mathbf{R} = \mathbf{e} \wedge \mathbf{L_1 e} \tag{16}$$

The axis of rotation $\mathbf{R}$ is given by the direction of the non-rotating filament, i.e. $\mathbf{e} \wedge \mathbf{L_1 e} = \mathbf{0}$ where $\mathbf{e}$ is the real eigenvector of the tensor $\mathbf{L_1}$. The rotation can then be studied in a plane perpendicular to $\mathbf{R}$, so in 2D. The details of the calculation are given in the section Appendix 6. When associated with the triple decomposition, the vortex has been called rortex Gao & Liu (2018). This is the the criterion that will be used in the paper for ECS detection.

With respect to the objectivity of the vortices defined in this way, they can all be made objective by subtracting a reference vortex. For example, the reference vortex can be a local average as for Haller's instantaneous vorticity deviation (IVD) (Haller *et al.* (2016)). Another proposal was the rotation of the eigenvector basis of the symmetric part $\mathbf{S_1}$ (see e.g. Martins *et al.* (2016)) for the Q criterion, but it has been proved that this criterion is still not objective (Haller (2021)). Another possibility would be to calculate the Laplacian of the rortex intensity. These criteria do not describe the real rotation of a filament anymore. Another approach, proposed in Günther & Theisel (2018), is to compute an optimal local reference frame to observe the flow. This reference frame is optimal in the sense that, in it, the velocity field should be locally as stable as possible.

3.3 Lagrangian Coherent Structures (LCS): spatio-temporal coherence

Eulerian coherent structures (ECS) describe collective behavior at very short times. But this observation can be biased in the sense that these behaviors can have a very short lifetime. LCS take into account a history (during an observation time T) to consider the future of specific events. The literature on this subject has grown exponentially over this century. In this article, not all ideas concerning LCS will be exposed. The interested reader can consult the articles Haller (2015), Santitissadeekorn *et al.* (2010), Lekien *et al.* (2007), Balasuriya *et al.* (2018). Several approaches have been used to identify LCS. For example, in Ma & Bollt (2015) or in Braun *et al.* (2006), they considered the characteristics of particle trajectories such as curvature to identify LCS. In Blazevski & Haller (2014), they defined hyperbolic, elliptical, or parabolic LCS as structures that lead to maximum deformation. Finite-time Lyapunov exponents (FTLE) are often used to distinguish between LCS (see Raben *et al.* (2014) for an experimental approach). Another practical approach is the use of Lagrangian descriptors (see for example Lopesino *et al.* (2017)). In fact, there is a close connection between mixing and LCSs, as hyperbolic LCSs can be considered as (quasi) transport barriers. Elliptical LCS can also be considered as sets of particles that stay together for a long time: this approach has been used by Froyland & Padberg (2009) to define almost invariant sets, or in Gouillart *et al.* (2009) to study strange eigenmodes.

In this paper, two criteria are used to study the spatio-temporal coherence of the flow: the FTLE and the Lagrangian descriptors. To calculate the trajectories, a Runge-Kutta 45 algorithm was used. When a trajectory went outside the computational domain, the velocity was set to zero. Lagrangian coherent structures are not very sensitive to noise, and in particular, the most intense structures are robust. To understand the Lagrangian criteria, let us introduce some quantities:

- $\boldsymbol{\phi}(\mathbf{x_0}, t_0, t)$ is the flux map. It gives the position of a particle at time t, which was initially in $mathbfx_0$ at time t_0.
- $\mathbf{F_1}$ is the gradient of the flow map. It can be obtained for example by integration of the differential equation $\dot{\mathbf{F}}_\mathbf{1} = \mathbf{L_1 F_1}$.
- The stretching of a filament is $eta = fracss_0 = \sqrt{\mathbf{t_0} \cdot \mathbf{C_1 t_0}}$ où $\mathbf{C_1} = \mathbf{F_1}^*\mathbf{F_1}$ is the Cauchy-Green tensor, and * is the transposition operator.
- The FTLE Λ_t^{t+T} is defined as follows: $\Lambda_t^{t+T} = \frac{1}{T}\ln(\lambda_{\max}(\mathbf{C_1}))$ where $\lambda_{\max}(\mathbf{C_1})$ is the largest eigenvalue of $\mathbf{C_1}$, T is the integration time.

The FTLE describes the exponential speed of separation of two trajectories that were initially very close. It is possible to define the FTLE Λ_t^{t-T} for a negative integration time $(-T)$. It can be calculated by reversing the direction of time. It describes the exponential rate of convergence of two initially distant trajectories.

- A Lagrangian descriptor $I_t^{t+T}(Q)$ of a quantity Q is the average of Q along the trajectory. $I_t^{t+T}(Q) = \frac{1}{T}\int_t^{t+T} Q(\boldsymbol{\phi}(\mathbf{x_0}, t, t'))\,dt'$. Examples of Q quantities of interest are the rortex norm or velocity norm. In this paper, the rortex is used and the corresponding Lagrangian descriptor is denoted R_L. It represents the average along a trajectory of the minimum rotation of the filament (see section 3.2).

4 Results

To investigate the information that could be obtained from one-point measurements, the time evolution of the three velocity components, extracted from the velocity fields, is presented in figure 5, for a initial height y/d_1=0,5. At the dimensionless time $t(g/d_1)^{1/2}$=0, the jump is at its maximum height. The u/U_1 velocity component decreases drastically (from 1 to 0,35 in a time around 5,9). At the same time, the v component is increasing to 0.17 and then decreases back to its initial zero value. Fluctuations in w increase slightly. Several measurements are made, for different initial positions of the sensor. Signals start at the same distance from the jump front. The time series are very different after the jump, which means that the process is entirely transient. Therefore, classical statistics (velocity average, ...) cannot be calculated during the whole process, because the results would depend on the observation time. Conventionnally, only a sliding window average could be considered. The fluctuations for y/d_1=0,5 are the smallest, since the measurement is outside the boundary and the shear layers. As the free surface is moving at a constant speed in the measurement zone, an average flow can be computed in the jump frame, by considering some kind of Taylor's hypothesis. It is possible to compute statistics in this frame, using the averaging operator given in equation 17.

$$< U >_b (\mathbf{X}) = \frac{1}{T}\int_0^T u(\mathbf{X} + \mathbf{U_b}t,\, t)\,dt \tag{17}$$

In the following part of the paper, the averages are in capital, and the fluctuations in small letters with a prime. For example, $U =< u >_b$ and $u' = u - U$. $u_{\mathrm{RMS}} = \sqrt{< u'^2 >_b}$ is the velocity average fluctuation in the jump frame. $u'v' =< (u-U)(v-V) >_b$ is the Reynolds stress calculated in the jump frame.

Let's consider for example the time evolution of the $u'v'/U_1^2$ fluctuations, respectively in the boundary layer (y/d_1=0,15) and in the shear layer (y/d_1=1,25) (figures 6 and 7), for several observation positions (from x/d_1=0 to 4). In this spatio-temporal representation, the position is shifted in order to align the data in time on the jump front.

From these figures, it is clear that there are fluctuations which propagate in the flow at a constant speed. They are mostly negative in the boundary layer and mostly positive in the shear layer. The passage of the jump induces strong fluctuations which attenuate after about twenty time units. The temporal averages are presented in figures 8 and 9.

They were computed for the components u, v, w and also the components of the Reynolds stress tensor $u'v'$, $u'w'$ and $v'w'$. The means and RMS values are shown. The statistics are calculated in the jump frame, which is why the domain in x is wider than the one being measured. The flow deceleration is clear on the longitudinal velocity component. A significant effect is visible on the boundary layer which thickens after the jump front. There is a negative velocity under the jump. A central core is visible, where the velocity is almost uniform after two undulations. It corresponds to a region of weak fluctuations in velocity. Undulations of the free surface are visible. They generate oscillations in the velocity field, due to the conservation of the flow rate. The vertical component shows even sharper oscillations: after a sharp increase in velocity under the jump, the vertical velocity is alternately positive and negative. The component W is very weak before the jump (2D flow) but the velocity becomes distinctly three-dimensional in the shear layer. The three velocity fluctuation fields are very similar: they show strong velocity fluctuations in the shear layer but also in the boundary layer. These fluctuations are of the same magnitude in all three directions. As indicated previously, the values $u'v'$ are mostly positive in the shear layer and negative in the boundary layer. The constraints in the boundary layer are less sharp in $v'w'$ and $u'w'$. In the shear layer, the stresses are important, especially for $u'w'$. Since the dominant fluctuations are along x, the constraints $u'v'$ and $u'w'$ last longer behind the front. Even if the statistical results give more information on the structuring of the flow, this is still quite limited and masks the spatio-temporal complexity of the flow. That is why Lagrangian analysis tools are interesting for studying the spatio-temporal coherence of the flow. The structures of strong rotation are displayed using the fields of the Lagrangian descriptor R_L. The integration time (used

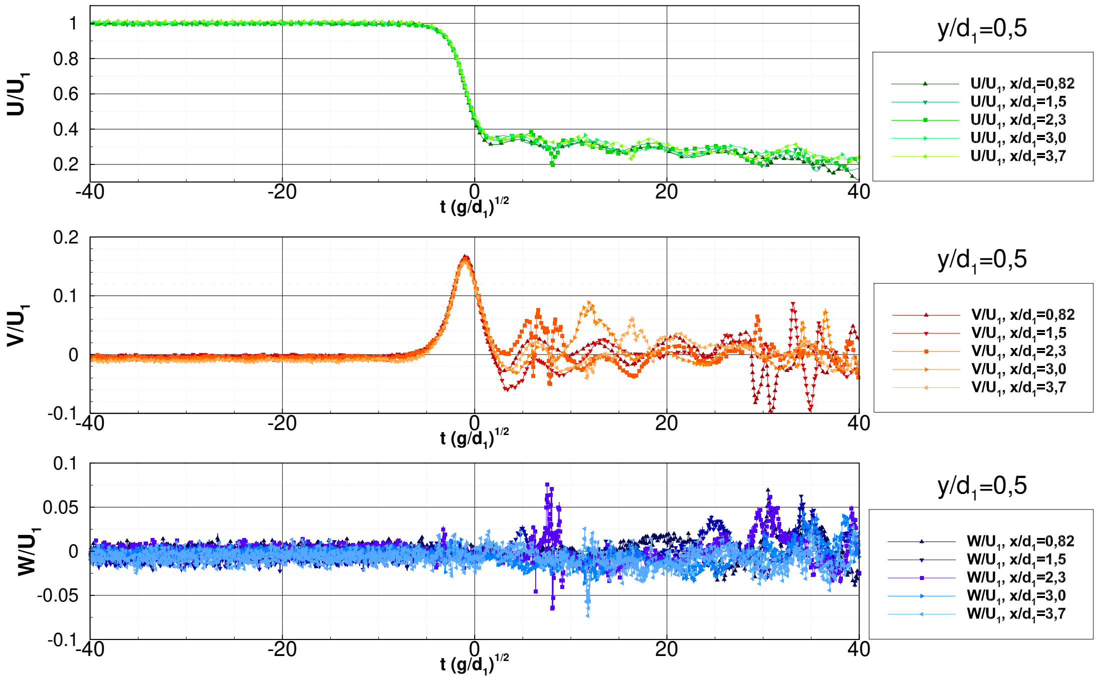

Fig. 5: Time evolution of the three velocity components for $\frac{y}{d_1}$=0,5, taken at different x/d_1 positions. In each case, the time origin is fixed when the vertical velocity is maximal.

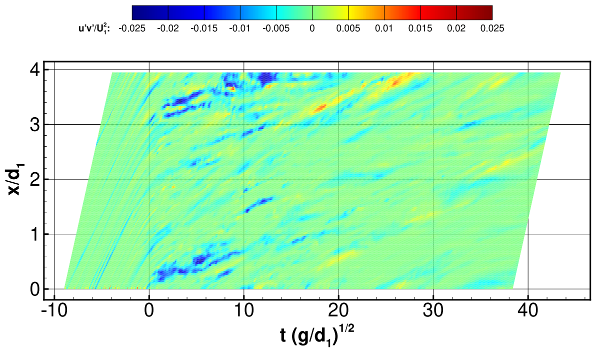

Fig. 6: Spatio-temporal diagram of the fluctuations $u'v'$ in the boundary layer $\frac{y}{d_1}$=0,15. For each x/d_1 position, the time is shifted in order that the origin correspond to a vertical velocity maximum.

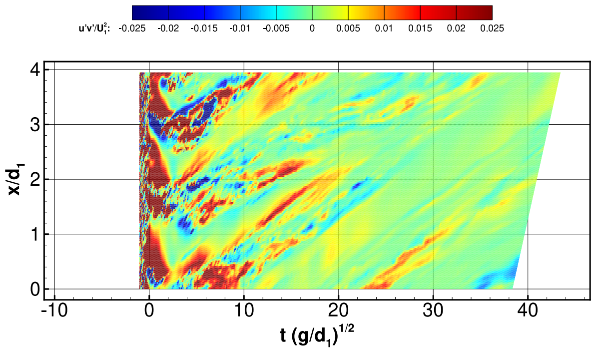

Fig. 7: Spatio-temporal diagram of the fluctuations $u'v'$ in the shear layer $\frac{y}{d_1}$=1,25. For each x/d_1 position, the time is shifted in order that the origin correspond to a vertical velocity maximum.

to calculate R_L) is chosen according to figure 10. In this figure, $R_{L,\min}$ and $R_{L,\max}$ are respectively the minimum and maximum values of R_L in the field. The curves give the evolution of these values with the integration time. The chosen integration time $T(g/d_1)^{1/2} = 1\ 835$ leads to the highest values of $|R_{L,\min}|$ and $|R_{L,\max}|$. The influence of the integration time is shown in figure 11. For short integration times, many structures are visible. They are similar to Eulerian structures. As the integration time increases, some structures disappear because their lifespan is shorter, and at the same time, some structures are getting stretched and less intense filamentous structures appear. However, on the whole, the strongest structures remain mostly unchanged.

The same approach can be used to choose the integration time for the FTLE but the choice is less clear

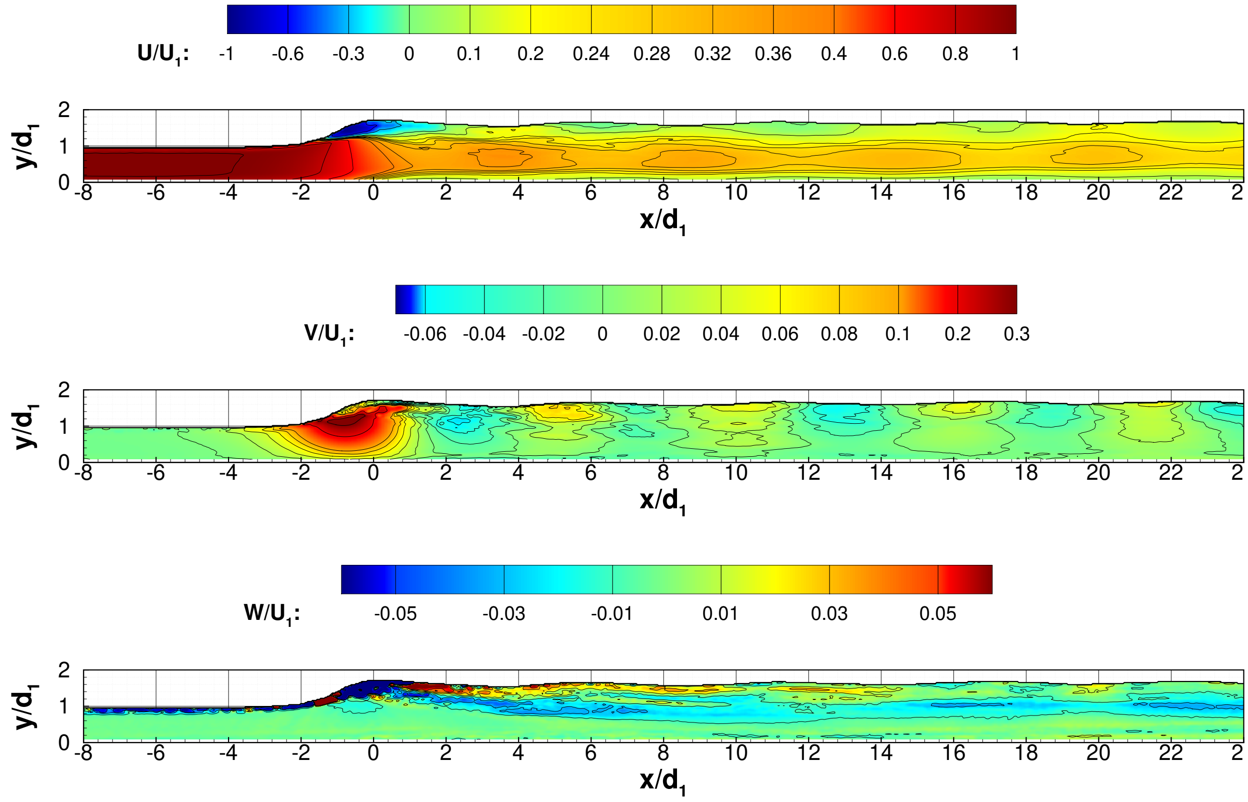

Fig. 8: Mean velocity fields computed in the hydraulic jump frame.

and more personal. The FTLE fields are presented for 3 different integration times in figure 12 (left part (a), (c) and (e)). The first integration time (a) is too short: the LCS do not appear clearly. The two other integration times give similar results except that small details appear for a longer integration time (e). They are not useful for the analysis and the choice of a shorter integration time leads to a faster computation (around 10 min per field). Finally, the integration time is fixed to $T(g/d_1)^{1/2}$=6,5. As the details being very thin, the spatial resolution must be high. This is why a self-adapting grid approach was used in order to reduce the computation time. At level 0, the grid is 32×32. When the level is increased, each cell in the grid is cut into four smaller cells (if the interpolation error is too large). The calculation is performed in parallel on several CPUs. The choice of the mesh is shown in figure 12 (right part (b), (d) and (f)). A number of nodes around 820 000 (level 5) is a good compromise for the representation.

The Lagrangian criteria (R_L, Λ_t^{t+T} and Λ_t^{t-T}) are combined in a single representation in figure 13. The temporal evolution of the LCS is presented for a duration of 5,208 during which the jump traverses the measurement zone, in 17 instants. Red iso-contours show positive FTLE, blues, negative FTLE, while the color map represents rotation (yellow – clockwise; green – counterclockwise). The uniform gray value represents the area where experimental data could be obtained. The purple circle follows a specific event in time. First of all, it is clear from the figures that the jump causes a dramatic change in the flow, in particular on the stability of the trajectories (red lines). Due to the high shear between the main flow and the jump, the flow is divided into a stagnation zone and a main flow region. The border between these two areas is not completely clear because the shear layer is destabilized, leading to the formation of powerful vortices. Another indication of the presence of these vortices is the crossing of the red and blue lines: these are the generalization of hyperbolic points for unsteady flows, characterized by stable (red) and unstable (blue) manifolds. Vortex pairs are also characterized by FTLE contours with a “jellyfish” shape. The blue “tentacles” represent fluid that follow the vortex pair and that is sucked in while red ones represent fluid that meets and bypass the pair. An example of such a structure can be found inside the circle drawn in each sub-figure. At first, the vortex pair is formed

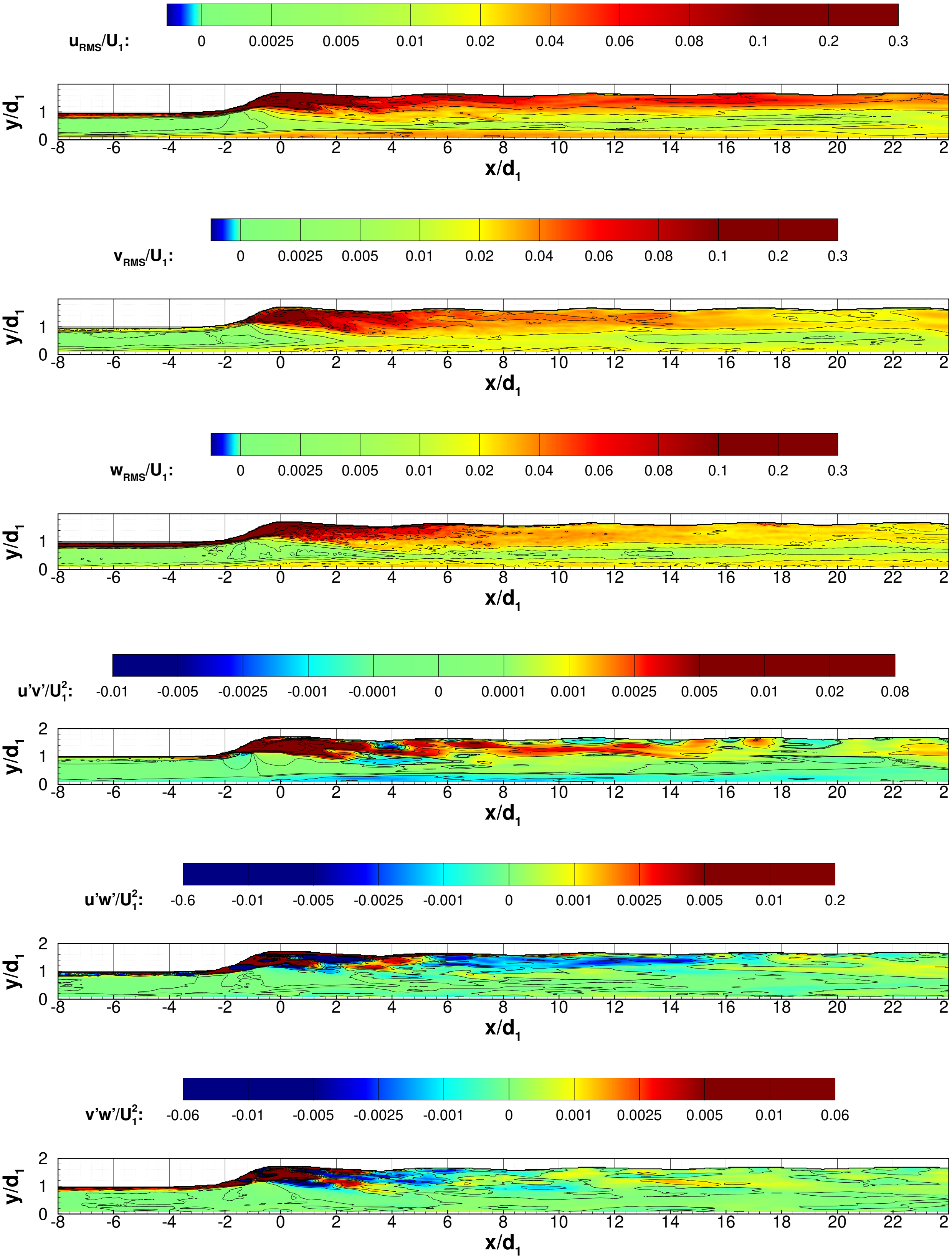

Fig. 9: Statistics of velocity fluctuations statistics computed in the hydraulic jump frame.

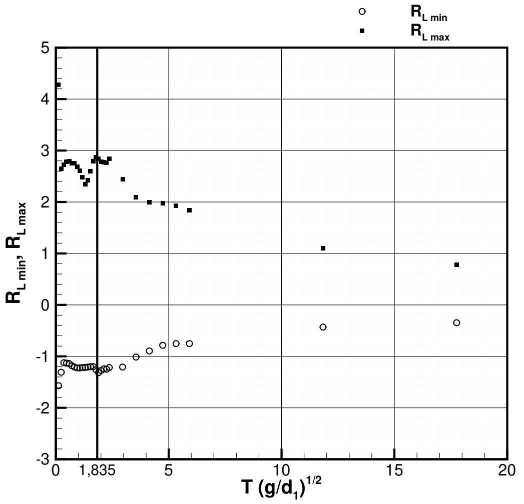

Fig. 10: Choice of the integration time T for the R_L computation. $R_{L,\min}$ and $R_{L,\max}$ are respectively the minimum and the maximum of the R_L field values. They are represented as a function of the dimensionless integration time. The retained value of $T(g/d_1)^{1/2}$=1,835 corresponds to the highest absolute values of $R_{L,\min}$ and $R_{L,\max}$.

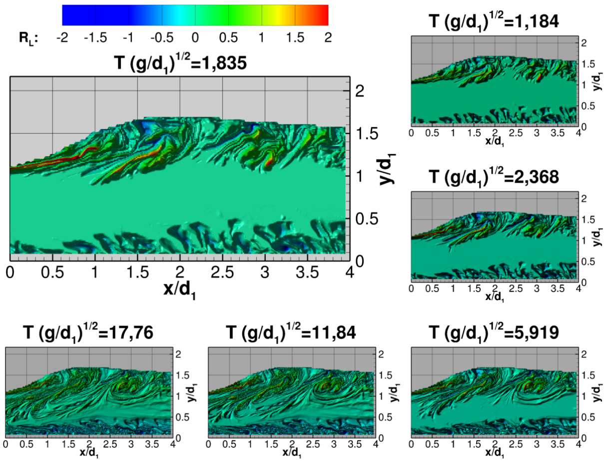

Fig. 11: Influence of the time integration on the rotation R_L.

from the fluid trapped between the jump front and the shear layer. Initially, it follows the jump, then when it is well formed, the self-induced velocity causes the vortex pair to descend in the flow, in a region where the main velocity is stronger and in a the main stream direction. The vortex pair is then drawn along the main flow. At the same time, the boundary layer thickens, there are more structures and they become more intense.

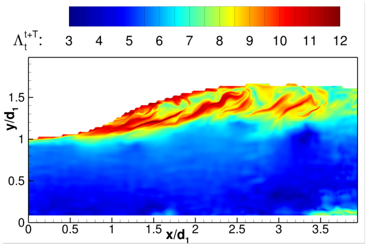

(a) $T(g/d_1)^{1/2}$=1,2; level 5

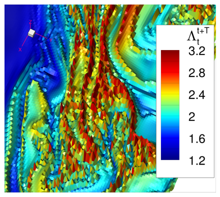

(b) $T(g/d_1)^{1/2}$=6,5
level 4
0,25·10^6 nodes

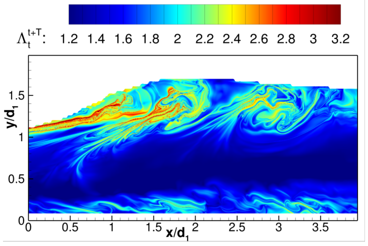

(c) $T(g/d_1)^{1/2}$=6,5; level 5

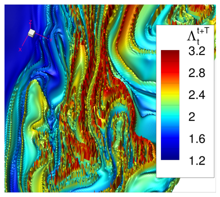

(d) $T(g/d_1)^{1/2}$=6,5
level 5
0,82·10^6 nodes

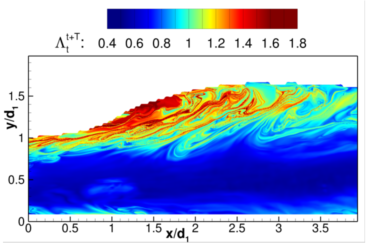

(e) $T(g/d_1)^{1/2}$=12; level 5

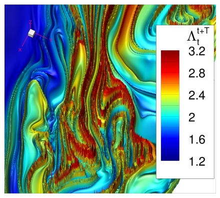

(f) $T(g/d_1)^{1/2}$=6,5
level 6
2,4·10^6 nodes

Fig. 12: Influence of the integration time on the FTLE fields, and of the grid resolution on the positive FTLE field Λ_t^{t+T}. **On the left** – (a), (c) and (e): zoom on a complex FTLE region. Integration time $T(\frac{g}{d_1})^{1/2}$ increasing from 1,2 to 12 and grid resolution at level 5 (0,82·10^6 nodes). **On the right** – (b), (d) and (f): integration time $T(\frac{g}{d_1})^{1/2}$=3,6 and increasing grid resolution from level 4 (0,25·10^6 nodes) to level 6 (2,4·10^6 nodes).

Another vision of temporal evolution is given in figure 14. It is about a spatio-temporal view of the rotation R_L, in the jump frame, with two spatial dimensions and one temporal. The time t=0 is set for the maximum water elevation. The (a) view is a side view of the flow. The red iso-surface corresponds to $R_L(g/d_1)^{-1/2}$=0,2, while the blue one corresponds to $R_L(g/d_1)^{-1/2}$=-0,1. The (b) view shows a bottom view. The R_L iso-surfaces are colored by the y/d_1 variable (varying from 0 to 0,5). The structures are inside the boundary layer. Finally, view (c) is also a bottom view, but for $y/d_1 > 0{,}5$. The green levels represent the free surface. In view (a), the thickening of the boundary layer is clear. The appearance of coherent structures is also clear behind the jump. The boundary layer evolution is visible in view

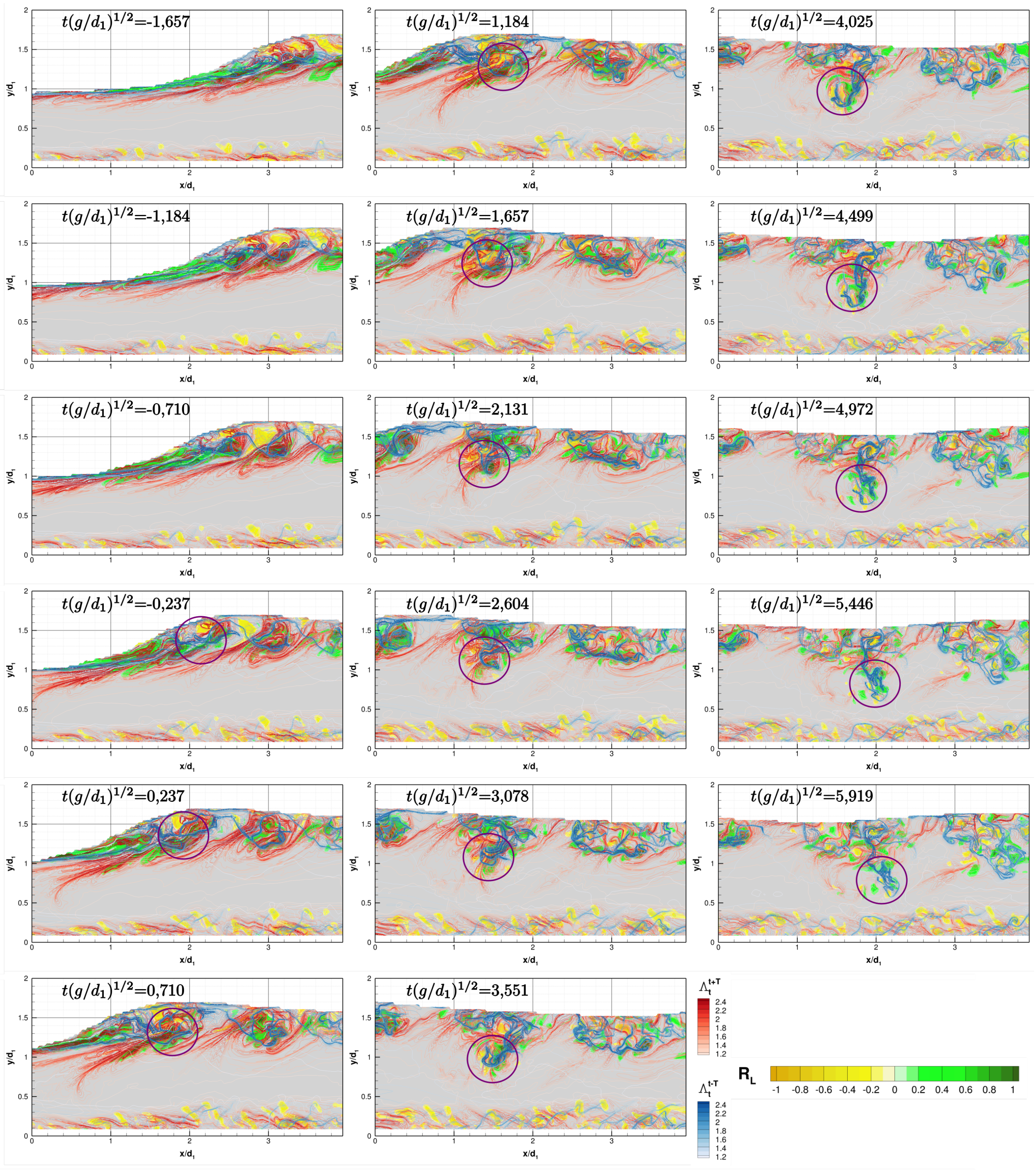

Fig. 13: Temporal evolution of the LCS (R_L colour iso-surface, FTLE red (positive time) and blue (negative time) iso-contours) for 17 consecutive instants, separated by $t\ (g/d_1)^{1/2}$=0,474.

(b). The coherent vortices velocity changes drastically behind the jump. This is due to the overall deceleration of the flow due to the increase in water depth. The velocity varies slightly with altitude. The shear layer dynamics is also clearly visible in view (c). Behind the jump, coherent vortices appear regularly (shear layer destabilization). In the laboratory frame, the structures seem immobile. During this stage, opposite vortices interact with this primary instability. After a while, the velocity increases and the structures move away from the jump. The vortices are quickly broken. The positive and negative structures intertwine and appear to rotate slightly around each other, but overall, their velocity is stable. They go deeper and deeper in the flow.

5 Conclusion

The results presented in this article show that 2D measurements improve the ability to analyze the flow: the flow organization can be directly observed while with 1D measurements, it can only be deduced from statistics such as correlations. It is especially true when the flow is unsteady. The spatial coherence of the flow can be observed through the Eulerian coherent structures. When the measurements are time resolved, the dynamics of the flow can be studied. The space-time coherence can be identified using Lagrangian coherent structures. Concerning the positive surge for a Froude around 1,5 studied in this paper, the main results are:

- The surge is undulating, partially breaking. It is 2D, except behind the front where even the mean W component is non-zero and in the boundary layer where the fluctuations w_{RMS} are positive.
- On average, the boundary layer thickens at the passage of the surge, and there is a shear layer below the free surface, which also invades the flow above the upstream water depth.
- The boundary layer contains coherent structures that are amplified by the upwelling and gradually invade the upper part of the flow. These structures are also slowing down.
- As the front angle is too high, the shear layer detaches from the free surface and then is destabilized, leading to the formation of coherent vortices. These vortices interact with the roller behind the front and form pairs (or sets) of vortices that rotate around each other and descend into the main stream. They accelerate and small structures are invading the entire flow, establishing a connection with the boundary layer.

The fluid mixing scenario is clearer now for this flow. The coherence tools introduced in this article brings new analyzing capacities. New quantities could be followed during a parametric study, such as the maximal penetration depth of the coherent structures formed behind the surge front, the frequency of the coherent structures creation, or their velocity. But there are still open questions. The flow is 3D, as shown by the w values, but the 3D organization of the flow is not clear. Strong vortices are generated but the destabilization mechanisms should be scrutinized. And it would be essential to quantify and understand the impact of the coherent structures on a sediment bed or on the walls.

References

Balasuriya S, Ouellette NT, Rypina II (2018) Generalized Lagrangian coherent structures. doi:10.1016/j.physd.2018.01.011

Blazevski D, Haller G (2014) Hyperbolic and elliptic transport barriers in three-dimensional unsteady flows. Physica D: Nonlinear Phenomena 273-274:46 – 62. doi:https://doi.org/10.1016/j.physd.2014.01.007

Braun W, De Lillo F, Eckhardt B (2006) Geometry of particle paths in turbulent flows. Journal of Turbulence 7(62):1–10. doi:10.1080/14685240600860923

Chanson H (2008) Acoustic doppler velocimetry (adv) in the field and in laboratory: Practical experiences. Tech. Rep. CH70/08, The University of Queensland, Division of Civil Engineering

Chanson H (2009) Current knowledge in hydraulic jumps and related phenomena. a survey of experimental results. European Journal of Mechanics - B/Fluids 28(2):191 – 210. doi:https://doi.org/10.1016/j.euromechflu.2008.06.004

David L, Chatellier L, Calluaud D, Jeon Y, Rousseaux G, Thomas L (2014) Tr-piv measurements in open channel flow for the analysis of undular tidal bores. In 17th International Symposium on Applications of Laser Techniques to Fluid Mechanics, Lisbon, Portugal

Epps B (2017) Review of Vortex Identification Methods. In 55th AIAA Aerospace Sciences Meeting. American Institute of Aeronautics and Astronautics. doi:10.2514/6.2017-0989

Froyland G, Padberg K (2009) Almost-invariant sets and invariant manifolds - Connecting probabilistic and geometric descriptions of coherent structures in flows. Physica D: Nonlinear Phenomena 238(16):1507–1523. doi:10.1016/j.physd.2009.03.002

Furgerot L, Mouazé D, Tessier B, Perez L, Haquin S, Weill P, Crave A (2016) Sediment transport induced by tidal bores. An estimation from suspended matter measurements in the Sée River (Mont-Saint-Michel Bay, northwestern France).

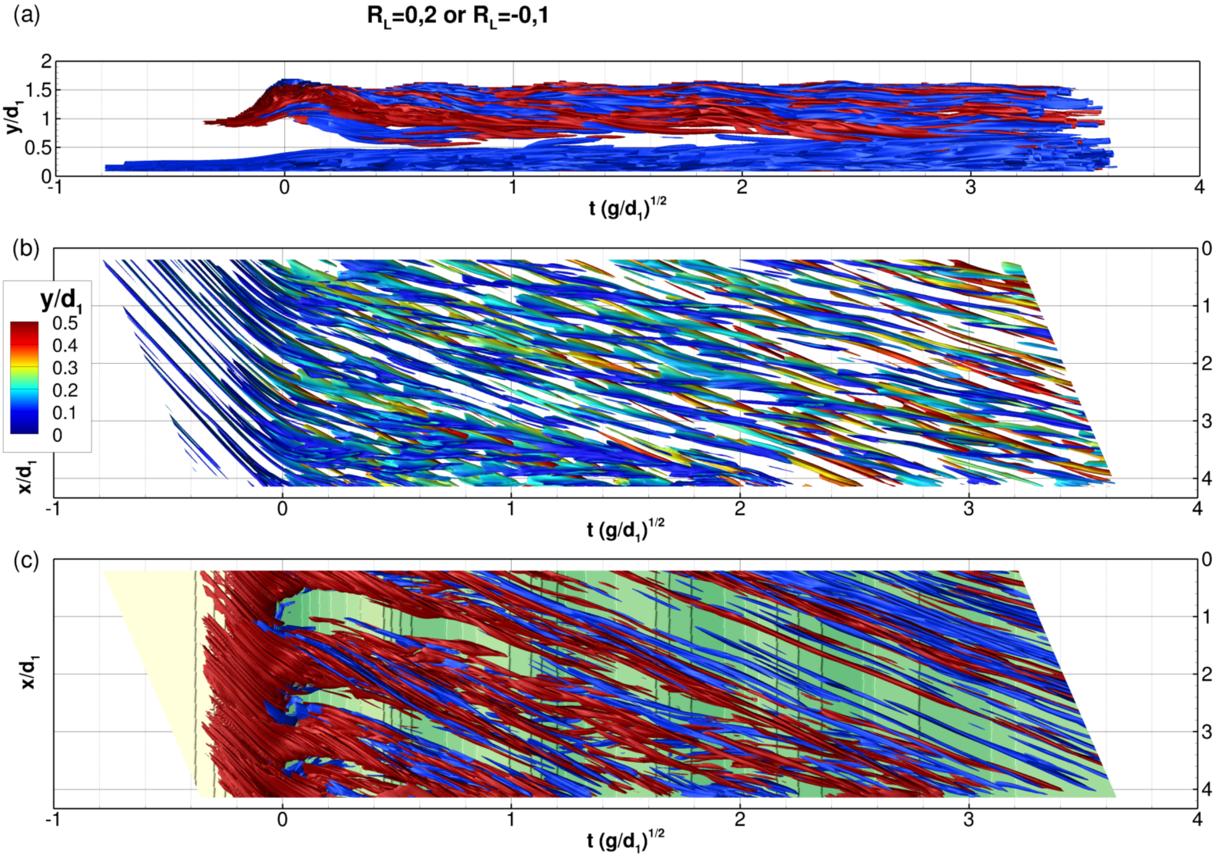

Fig. 14: Spatio-temporal diagram showing the time evolution of the LCS R_L. The top view (a) is a side view of the Rotation iso-contours, colored by rotation (blue, R_L=-0,1; red, R_L=0,2). The middle view (b) represents iso-contours of Rotation that are under y/d_1=0,5, viewed from bottom and colored by height. The bottom view (c) shows iso-contours of Rotation that are above y/d_1=0,5, viewed from under the free surface (shown in yellow/green) and colored by Rotation (blue, R_L=-0,1; red, R_L=0,2).

Comptes Rendus Géoscience 348(6):432–441. doi: 10.1016/j.crte.2015.09.004. (IF 1.54; Q2)

Gao Y, Liu C (2018) Rortex and comparison with eigenvalue-based vortex identification criteria. arXiv:180503984 [physics] ArXiv: 1805.03984

Gouillart E, Dauchot O, Thiffeault JL, Roux S (2009) Open-flow mixing: Experimental evidence for strange eigenmodes. Physics of Fluids 21(2):023603. doi: 10.1063/1.3080680

Grant HL (1958) The large eddies of turbulent motion. Journal of Fluid Mechanics 4(02):149. doi: 10.1017/S0022112058000379

Günther T, Theisel H (2018) Hyper-objective vortices. IEEE Transactions on Visualization and Computer Graphics 1–1. doi:10.1109/TVCG.2018.2868760

Günther T, Theisel H (2018) The State of the Art in Vortex Extraction: The State of the Art in Vortex Extraction. Computer Graphics Forum doi: 10.1111/cgf.13319

Haller G (2005) An objective definition of a vortex. Journal of Fluid Mechanics 525:1–26. doi: 10.1017/S0022112004002526

Haller G (2015) Lagrangian Coherent Structures. Annual Review of Fluid Mechanics 47(1):137–162. doi: 10.1146/annurev-fluid-010313-141322

Haller G (2021) Can vortex criteria be objectivized? Journal of Fluid Mechanics 908. doi: 10.1017/jfm.2020.937

Haller G, Hadjighasem A, Farazmand M, Huhn F (2016) Defining coherent vortices objectively from the vorticity. Journal of Fluid Mechanics 795:136–173. doi:10.1017/jfm.2016.151

Hornung HG, Willert C, Turner S (1995) The flow field downstream of a hydraulic jump. Journal of Fluid Mechanics 287:299–316. doi: 10.1017/S0022112095000966

Hussain AKMF (1983) Coherent structures—reality and myth. Physics of Fluids 26(10):2816. doi:

10.1063/1.864048

Jeon YJ, Chatellier L, David L (2014) Fluid trajectory evaluation based on an ensemble-averaged cross-correlation in time-resolved PIV. Experiments in Fluids 55(7). doi:10.1007/s00348-014-1766-9

Jeong J, Hussain F (1995) On the identification of a vortex. Journal of Fluid Mechanics 285(-1):69. doi:10.1017/S0022112095000462

Koch C, Chanson H (2008) Turbulent mixing beneath an undular bore front. Journal of Coastal Research 24(4):999–1007. doi:10.2112/06-0688.1

Kolář V (2007) Vortex identification: New requirements and limitations. International Journal of Heat and Fluid Flow 28(4):638–652. doi:10.1016/j.ijheatfluidflow.2007.03.004

Lekien F, Shadden SC, Marsden JE (2007) Lagrangian coherent structures in n-dimensional systems. Journal of Mathematical Physics 48(6):065404. doi:10.1063/1.2740025

Leng X, Chanson H (2016) Coupling between free-surface fluctuations, velocity fluctuations and turbulent reynolds stresses during the upstream propagation of positive surges, bores and compression waves. Environmental Fluid Mechanics 16(4):695–719. doi:10.1007/s10652-015-9438-8

Leng X, Chanson H (2017a) Integral turbulent scales in unsteady rapidly varied open channel flows. Experimental Thermal and Fluid Science 81:382 – 395. doi:10.1016/j.expthermflusci.2016.09.017

Leng X, Chanson H (2017b) Unsteady turbulence, dynamic similarity and scale effects in bores and positive surges. European Journal of Mechanics - B/Fluids 61:125 – 134. doi:https://doi.org/10.1016/j.euromechflu.2016.09.017

Lennon JM, Hill DF (2006) Particle image velocity measurements of undular and hydraulic jumps. Journal of Hydraulic Engineering 132(12):1283–1294. doi:10.1061/(ASCE)0733-9429(2006)132:12(1283)

Liu JTC (1989) Coherent Structures in Transitional and Turbulent Free Shear Flows. Annual Review of Fluid Mechanics 21(1):285–315. doi:10.1146/annurev.fl.21.010189.001441

Lopesino C, Balibrea-Iniesta F, García-Garrido VJ, Wiggins S, Mancho AM (2017) A Theoretical Framework for Lagrangian Descriptors. International Journal of Bifurcation and Chaos 27(01):1730001. doi:10.1142/S0218127417300014

Lubin P, Chanson H (2017) Are breaking waves, bores, surges and jumps the same flow? Environmental Fluid Mechanics 17:47 – 77. doi:10.1007/s10652-016-9475-y

Lubin P, Glockner S, Chanson H (2010) Numerical simulation of a weak breaking tidal bore. Mechanics Research Communications 37(1):119–121. doi:https://doi.org/10.1016/j.mechrescom.2009.09.008

Ma T, Bollt EM (2015) Shape Coherence and Finite-Time Curvature Evolution. International Journal of Bifurcation and Chaos 25(05):1550076. doi:10.1142/S0218127415500765

Martin JPV, Dolz J, Del Estal J (1993) Kinematics of the moving hydraulic jump. Journal of Hydraulic Research 31(2):171–186. doi:10.1080/00221689309498843

Martins RS, Pereira AS, Mompean G, Thais L, Thompson RL (2016) An objective perspective for classic flow classification criteria. Comptes Rendus Mécanique 344(1):52 – 59. doi:https://doi.org/10.1016/j.crme.2015.08.002

Raben SG, Ross SD, Vlachos PP (2014) Experimental determination of three-dimensional finite-time Lyapunov exponents in multi-component flows. doi:10.1007/s00348-014-1824-3

Raffel M, Willert CE, Scarano F, Kähler CJ, Wereley ST, Kompenhans J (2018) Particle Image Velocimetry. Springer International Publishing, Cham. doi:10.1007/978-3-319-68852-7

Santitissadeekorn N, Froyland G, Monahan A (2010) Optimally coherent sets in geophysical flows: A transfer-operator approach to delimiting the stratospheric polar vortex. Physical Review E 82(5):056311. doi:10.1103/PhysRevE.82.056311

Wüthrich D, Shi R, Chanson H (2020) Physical study of the 3-dimensional characteristics and free-surface properties of a breaking roller in bores and surges. Experimental Thermal and Fluid Science 112:109980. doi:https://doi.org/10.1016/j.expthermflusci.2019.109980

Yeh HH, Mok K (1990) On turbulence in bores. Physics of Fluids A: Fluid Dynamics 2(5):821–828. doi:10.1063/1.857630

Zheng F, Li Y, Xuan G, Li Z, Zhu L (2018) Characteristics of positive surges in a rectangular channel. Water 10:1473. doi:10.3390/w10101473

6 Appendices

6.1 $\mathbf{L_1}$ diagonalization

The matrix $\mathbf{L_1}$ can be diagonalized in $\mathbb{C}$. The characteristic polynomial of the matrix is $\lambda^3 + P\lambda^2 + Q\lambda + R$ with P, Q and R defined in the equations 18, 19 and 21.

$$P = -\mathrm{div}\mathbf{u} = -(L_{11} + L_{22} + L_{33}) \tag{18}$$

$$Q = \frac{1}{2}\left(P^2 - \mathrm{tr}(\mathbf{L}_1^2)\right) = \frac{1}{2}\left(P^2 + ||\mathbf{W}_1||^2 - ||\mathbf{S}_1||^2\right)$$

(19)

or

$$Q = L_{11}L_{22}+L_{11}L_{33}+L_{22}L_{33}-L_{12}L_{21}-L_{13}L_{31}-L_{23}L_{32}$$

(20)

$$R = -\det\mathbf{L}_1 = \frac{1}{3}\left(-P^3 + 3PQ - \mathrm{tr}(\mathbf{L}_1^3)\right) \tag{21}$$

or

$$R = L_{11}L_{23}L_{32} - L_{11}L_{22}L_{33} + L_{12}L_{21}L_{33} - L_{12}L_{23}L_{31} + L_{13}L_{22}L_{31} - L_{13}L_{21}L_{32} \tag{22}$$

$$p = Q - \frac{1}{3}P^2 \tag{23}$$

$$q = R + \frac{2}{27}P^3 - \frac{1}{3}PQ \tag{24}$$

If q and p are defined in equations 23 and 24, the discriminant is $\Delta = \left(\frac{p}{3}\right)^3 + \left(\frac{q}{2}\right)^2$. If $\Delta > 0$, there is one real eigenvalue λ_r and two complex conjugated eigenvalues $\lambda_c = \lambda_{cr} + i\lambda_{ci}$ and $\overline{\lambda_c}$. The respective eigenvectors are $\mathbf{e_r}$, $\mathbf{e_c} = \mathbf{e_{cr}} + i\mathbf{e_{ci}}$ and $\overline{\mathbf{e_c}}$. The real form of the matrix in the basis $(\mathbf{e_{cr}}, \mathbf{e_{ci}}, \mathbf{e_r})$ is given in equation 25.

$$\mathbf{L_1} = \begin{pmatrix} \lambda_{cr} & \lambda_{ci} & 0 \\ -\lambda_{ci} & \lambda_{cr} & 0 \\ 0 & 0 & \lambda_r \end{pmatrix} \tag{25}$$

The eigenvalues are given by Cardano's formulas (equations 26, 27, 28, 29 and 30).

$$u = \left(-\frac{q}{2} - \sqrt{-\Delta}\right)^{\frac{1}{3}} \tag{26}$$

$$v = \left(-\frac{q}{2} + \sqrt{-\Delta}\right)^{\frac{1}{3}} \tag{27}$$

$$\lambda_r = -\frac{P}{3} + u + v \tag{28}$$

$$\lambda_{cr} = -\frac{P}{3} - \frac{u+v}{2} \tag{29}$$

$$\lambda_{ci} = \frac{\sqrt{3}}{2}(u - v) \tag{30}$$

The eigenvectors are given in equations 31, 32 and 33.

$$\mathbf{e_r} = \begin{pmatrix} L_{13}\lambda_r + L_{12}L_{23} - L_{22}L_{13} \\ L_{23}\lambda_r + L_{21}L_{13} - L_{11}L_{23} \\ \lambda_r^2 - (L_{11} + L_{22})\lambda_r + L_{11}L_{22} - L_{12}L_{21} \end{pmatrix} \tag{31}$$

$$\mathbf{e_{cr}} = \begin{pmatrix} 0 \\ -L_{13}L_{33} - L_{12}L_{23} - L_{11}L_{13} + 2\lambda_{cr}L_{13} \\ L_{13}L_{32} + L_{12}L_{22} + L_{11}L_{12} - 2\lambda_{cr}L_{12} \end{pmatrix} \tag{32}$$

$$\mathbf{e_{ci}} = -\frac{1}{\lambda_{ci}} \begin{pmatrix} L_{13}(L_{13}L_{32} - L_{12}L_{33}) + L_{12}(L_{13}L_{22} - L_{12}L_{23}) - \lambda_{cr}L_{12}L_{13} \\ L_{13}(L_{23}L_{32} - L_{22}L_{33}) + (L_{11} - \lambda_{cr})(L_{12}L_{23} - L_{13}L_{22}) + (L_{13}(L_{11} - \lambda_{cr}) + L_{33})\lambda_{cr} \\ L_{12}(L_{22}L_{33} - L_{23}L_{32}) + L_{11}(L_{12}L_{33} - L_{13}L_{32}) + (L_{13}L_{32} - 2L_{12}L_{33})\lambda_{cr} \end{pmatrix} \tag{33}$$

6.2 Orthogonalized eigenbasis for $\mathbf{L_1}$

The eigenvector basis is not orthogonal, and not normalized. It can be made direct (*i.e.* if $(\mathbf{e_{cr}} \wedge \mathbf{e_{ci}}) \cdot \mathbf{e_r} < 0$, the orientation of $\mathbf{e_{ci}}$ is changed). It is possible to normalize and orthogonalize the basis with the matrix $\mathbf{P}$, given in equation 34.

where $k_{rcr} = \mathbf{e_r} \cdot \mathbf{e_{cr}}$, $k_r = \mathbf{e_r} \cdot \mathbf{e_r}$, $k_{cr} = \mathbf{e_{cr}} \cdot \mathbf{e_{cr}}$, $k_{rci} = \mathbf{e_r} \cdot \mathbf{e_{ci}}$, $k_{ci} = \mathbf{e_{ci}} \cdot \mathbf{e_{ci}}$, $k_{cri} = \mathbf{e_{cr}} \cdot \mathbf{e_{ci}}$, $N_r = \sqrt{k_{cr} - \frac{k_{rcr}^2}{k_r}}$, $N_i = \sqrt{k_{ci} - \frac{k_{rci}^2}{k_r}}$ and $\alpha = \frac{k_{cri} - k_{rcr}k_{rci}}{N_r N_i}$

$$\mathbf{P} = \begin{pmatrix} \frac{1}{\sqrt{2(1+\alpha)}N_r} & \frac{1}{\sqrt{2(1-\alpha)}N_r} & 0 \\ \frac{1}{\sqrt{2(1+\alpha)}N_i} & -\frac{1}{\sqrt{2(1-\alpha)}N_i} & 0 \\ \frac{-\frac{k_r}{N_r} - \frac{k_i}{N_i}}{k_r\sqrt{2(1+\alpha)}} & \frac{\frac{k_i}{N_i} - \frac{k_r}{N_r}}{k_r\sqrt{2(1-\alpha)}} & \frac{1}{\sqrt{k_r}} \end{pmatrix} \tag{34}$$

$$\mathbf{P}^{-1} = \begin{pmatrix} \frac{\sqrt{1+\alpha}}{\sqrt{2}}N_r & \frac{\sqrt{1+\alpha}}{\sqrt{2}}N_i & 0 \\ \frac{\sqrt{1-\alpha}}{\sqrt{2}}N_r & -\frac{\sqrt{1-\alpha}}{\sqrt{2}}N_i & 0 \\ \frac{k_{rcr}}{\sqrt{k_r}} & \frac{k_{rci}}{\sqrt{k_r}} & \sqrt{k_r} \end{pmatrix} \tag{35}$$

The new form of the matrix in this orthonormal frame is given in equation 36.

$$\mathbf{L_1} = \begin{pmatrix} \lambda_{cr} + a\lambda_{ci} & -\frac{b}{c}\lambda_{ci} & 0 \\ bc\lambda_{ci} & \lambda_{cr} - a\lambda_{ci} & 0 \\ A & B & \lambda_r \end{pmatrix} \tag{36}$$

where $a = \frac{1}{2}\left(\frac{N_r}{N_i} - \frac{N_i}{N_r}\right)$, $b = \frac{1}{2}\left(\frac{N_r}{N_i} + \frac{N_i}{N_r}\right)$ and $c = \sqrt{\frac{1-\alpha}{1+\alpha}}$. The expressions of A and B are given below, but they are of no importance for the results.

$$A = \frac{(k_{rcr}N_r - k_{rci}N_i)\lambda_{ci} + (k_{rci}N_r + k_{rcr}N_i)\lambda_{cr} - (k_{rci}N_r + k_{rcr}N_i)\lambda_r}{\sqrt{2k_r(1+\alpha)}N_rN_i}$$

$$B = \frac{-(k_{rcr}N_r + k_{rci}N_i)\lambda_{ci} + (-k_{rci}N_r + k_{rcr}N_i)\lambda_{cr} + (k_{rci}N_r - k_{rcr}N_i)\lambda_r}{\sqrt{2k_r(1-\alpha)}N_rN_i}$$

In this frame, the values of γ, ω and σ are given in equations 37, 38 and 39.

$$\frac{\sigma}{2} = \lambda_{cr} \tag{37}$$

$$\frac{\omega}{2} = \frac{b}{2}\left(c + \frac{1}{c}\right)\lambda_{ci} \tag{38}$$

$$\gamma = \sqrt{a^2 + \left(\frac{b}{2}\right)^2\left(c - \frac{1}{c}\right)^2}|\lambda_{ci}| \tag{39}$$

There is a relation between ω, γ and λ_{ci}, given in equation (40).

$$\left(\frac{\omega}{2}\right)^2 - \gamma^2 = \lambda_{ci}^2 \tag{40}$$

The $Q_{2D}^{\frac{1}{2}} = \sqrt{(\frac{\omega}{2})^2 - \gamma^2}$ criterion is then equivalent to λ_{ci} criterion. Another formula to compute the rortex is given in equation (41), where $\omega_r = \boldsymbol{\omega} \cdot \mathbf{e_r}$.

$$\mathbf{R} = \left(\frac{\omega_r}{2} - \sqrt{\left(\frac{\omega_r}{2}\right)^2 - \lambda_{ci}^2}\right)\mathbf{e_r} \tag{41}$$

6.3 $\mathbf{L_1}$ robust estimation

When processing experimental data, noise becomes pregnant when computing derivatives. In this study, an original method has been used to reduce the noise on the estimation of $\mathbf{L_1}$. It is based on 4th order finite differences schemes, that are computed in different directions, on a grid box 5×5. For example, for a point inside the domain, the finite difference coefficients are $(\frac{1}{12}, -\frac{8}{12}, 0, \frac{8}{12}, -\frac{1}{12})$. (On the edges of the domain, the scheme is shifted to stay of 4th order.) The calculation of the x derivatives can be made by averaging the finite differences results in different directions. Taking into account the symmetries, it is possible to get 3 different values by averaging the following direction groups:

- $(1, 0)$
- $(1, 1)$ and $(1, -1)$
- $(1, 2)$ and $(1, -2)$

In order to reduce the noise, the median of these three values is taken, giving the derivative estimate.